Insight into the Gd–Pt Bond: Slow Magnetic Relaxation of a Heterometallic Gd–Pt Complex

Takefumi Yoshida,* [a,!] Ahmed Shabana,[a,b] Haitao Zhang,[a] David Chukwuma Izuogu,[c,d] Tetsu Sato,[a] Kentaro Fuku,[a] Hitoshi Abe,[e,f,g] Yoji Horii,[h] Goulven Cosquer,[i] Norihisa Hoshino,[j] Tomoyuki Akutagawa,[j] Alex J. W. Thom,[c] Shinya Takaishi,[a] and Masahiro Yamashita* [k, a]

[a] Department of Chemistry, Graduate School of Science, Tohoku University, 6-3 Aramaki-Aza-Aoba, Aoba-ku, Sendai 980-8578, Japan.

[b] Chemistry Department, Faculty of Science, Mansoura University, Mansoura, 35516, Egypt.

[c] Yusuf Hamied Department of Chemistry, University of Cambridge Lensfield Road, Cambridge, CB2 1EW, UK.

[d] Department of Pure and Industrial Chemistry University of Nigeria, Nsukka, 410001, Enugu State, Nigeria.

[e] Institute of Materials Structure Science High Energy Accelerator Research Organization (KEK) 1-1 Oho, Tsukuba, Ibaraki 305-0801, Japan.

[f] Department of Materials Structure Science, School of High Energy Accelerator Science, SOKENDAI(the Graduate University for Advanced Studies) 1-1 Oho, Tsukuba, Ibaraki 305-0801, Japan.

[g] Graduate School of Science and Engineering, Ibaraki University, 2-1-1 Bunkyo, Mito, Ibaraki 310-8512, Japan.

[h] Department of Chemistry, Nara Womens` University, Kitauoyanishimachi, Nara 630-8503, Japan.

[i] Department of Chemistry, Graduate School of Science Hiroshima University, 1-3-1 Kagamiyama, Higashihiroshima 739-8526, Japan.

[j] Institute of Multidisciplinary Research for Advanced Materials, Tohoku University, 2-1-1 Katahira, Aoba-ku, Sendai, Japan.

[k] School of Materials Science and Engineering Nankai University, Tianjin 300350, P.R. China.

! Innovation Research Center for Fuel Cells, The University of Electro-Communications, Chofu, Tokyo 182-8585, Japan

Corresponding Author

*Takefumi Yoshida. *Masahiro Yamashita. E-mail: takefumi.yoshida@uec.ac.jp, yamasita@agnus.chem.ac.jp

ABSTRACT

Lanthanide (Ln) compounds are common research targets in the field of magnetism and optics. Their properties arise from the electron localized in the f-orbital. Moreover, the effect of the covalency between lanthanide and ligands on magnetism attracted significant attention. We provided insight into the Gd–Pt bond (of the heterometallic Ln-Pt complexes: {[Pt(PhSAc)$_4$]Ln[(PhSAc)$_4$Pt]} NEt_4·2DMF (Ln = Y(**0**), La(**1**), Gd(**2**); PhSAc = thiobenzoate, NEt_4 = tetraethylammonium)); single-crystal polarized X-ray absorption near edge structure (XANES) reveal the electronic states around metal ion, where spectra of Gd-L_{III} edges show the Gd–Pt direction has the highest covalency (less ionic) around Gd ion in **2**. In addition, calculating natural bonding (NBO) analysis, natural population analysis (NPA), LOL, and atoms in molecules (AIM), *ab initio* calculations reveal the role of metallic and organic ligands in the electronic and magnetic properties of Ln complexes. The slow magnetization relaxation of the Gd complex, which has not been reported previously in the Pt–Gd–Pt system, was observed up to 45K, the highest temperature reported to date among isolated Gd-complexes.

TOC GRAPHICS

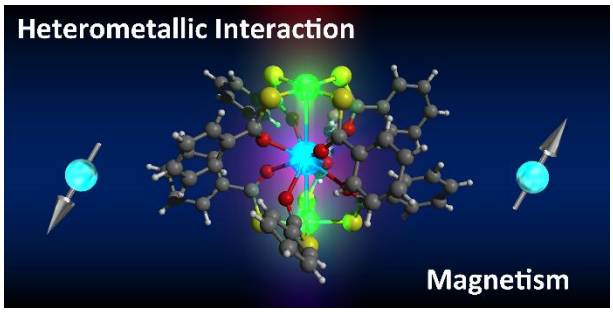

The study about the effect of the covalency between lanthanide and ligands on magnetism attracted significant attention. We synthesized the heterometallic Ln−Pt complexes, in which the diamagnetic Pt(II) ions interact with the Gd(III) ion. We evaluated the Ln−Pt bond. Also, this complex showed a slow magnetic relaxation up to 45K which is the highest temperature reported to date for an isolated Gd-complex.

KEYWORDS gadolinium, heterometallic bond, magnetic properties, slow magnetic relaxation

INTRODUCTION

The properties of lanthanide (Ln) compounds have made them prime research candidates in the field of magnetism,[1] optics,[2] and catalysis.[3] Control of magnetism and optical properties, which arise from the 4f electrons, is highly desired in materials science. The stereotypical understanding of the 4f electrons is often considered to be localized (core-like). They do not undergo large crystal fields (CF) splitting; thus, Ln(III) ions (except for Ce(III) or Ln(II) ions) in coordination complexes mainly behave like free ions.

Ln-based single-molecule magnets (SMMs) are a crucial subject for molecular spintronics, in which the molecular spin is utilized for information processing. Previous studies have shown that Dy complexes have strong magnetic anisotropies and large activation barriers (ΔE) of spin flipping among spin up and spin down states. As a result, Dy complexes have been developed as high-performance molecular magnets.[1a-h] Recently, organometallic Dy complexes that have a strong magnetic anisotropy or high symmetry around the Dy ion with a large ΔE, have been reported. In this system, a (weak) CF is a dominant source of the perturbation to resolve the degeneration of ground multiplet ($^6H_{15/2}$) so that the axial magnetic states are stabilized.[1a-c, 4, 5] Therefore, an electrostatic CF has been used to control the physical properties of the f-electrons. In addition, significant efforts have been made to enhance the features by changing the CF, magnetic interactions, and ligands.

In contrast, the reports in which the f orbital itself interacts with the orbitals of other atoms (s-f, p-f, d-f interaction) have been reported for intermetallics, metal oxides, and metal salts, and superconducting behavior was demonstrated in the 1980s.[6] Recently, Kuga *et al.* determined the exact model of hybridization among Yb 4f and B 2p on $YbAlB_4$.[6a]

However, recent studies have reassessed the covalency of Ln metal complexes.[7-11] La Pierre *et al.* reported the Tb(IV) complex stabilized by metal-ligand covalency.[7] On the other hand, Liddle *et al.* reported the heterometallic U–M complexes with an M–U bond (U: uranium, M: metal).[8a-c] Also, Hall *et al.* reported an unsupported Ln–Fe bond of $PyCp_2Ln\text{-}FeCp(CO)_2$ described as a dative bond.[8d] In addition, Totti *et al.* revealed the clear association between the covalent contribution of the coordinated water (which varied the quadrupolar potential) and the magnetic anisotropy of the Dy ion of $[Dy(DOTA)(H_2O)]^-$.[9] Although the details of the interaction between f-orbitals and ligands for other complexes are still unclear, the effect of the heterometal bonds needs to be considered when discussing the magnetic properties of heterometallic bonded systems. Thus, the perturbations caused by the nature of bonds cannot be ignored necessitating combined theoretical and experimental investigations.

Considering the difference in the size of the orbital and the electronegativity between the main group element and the transition metal element, it seems that the metallic ligand can enlarge the dative bond or covalency contribution. Bendix *et al.* estimated that minor changes in the orbital overlap among Ln and Pt/Pd affect the magnitude of zero magnetic fields splitting.[10a, 10h] On the other hand, the theoretical calculation (localized orbital locator (LOL) analysis) and experimental data (X-ray absorption spectra: XAS) of Ln–Pd and Ln–Pt complexes indicated the electron donation from the Pd and Pt ions to Ln.[10b, 10c] Electron spin resonance, luminescence spectra and inelastic neutron scattering are strong experimental methods to reveal the splitting of m_J states of Ln ion by fitting with the CF parameters.[10a,d,h] However, theoretical approaches should also be considered with the ligand field theory and covalency in calculating the splitting energies of the m_J states of Ln ions to circumvent the risk of overparameterization or wrong fitting value for systems involving a small splitting of the m_J states (especially in Gd ion).

In this work, insight into the Gd–Pt bond (of the heterometallic Ln–Pt complexes: {[Pt(PhSAc)$_4$]Ln[(PhSAc)$_4$Pt]} NEt_4·2DMF (Ln = Y(**0**), La(**1**), Gd(**2**); PhSAc = thiobenzoate, NEt_4 = tetraethylammonium)) was provided; single-crystal polarized X-ray absorption near edge structure (XANES) reveals the electronic states around the metal ion, where spectra of Gd-L_{III} edges show the Gd–Pt direction has the highest covalency (less ionic) around Gd ion in **2**. In addition, natural bonding (NBO) analysis, natural population analysis (NPA), LOL, atoms in molecules (AIM), and *ab initio* calculations revealed the role of metallic and organic ligands in the electronic and magnetic properties of Ln complexes. PhSAc ligand is bulky, increases the intermolecular distance, and is effective in suppressing magnetic and intermolecular interactions between the Ln ions. Furthermore, it is effective for adding optical characteristics such as luminescence. The slow magnetization relaxation of the Gd complex was observed up to 45K, whic is the highest temperature reported to date among isolated Gd-complexes.

RESULTS & DISCUSSION

Crystal Structure. The crystal structure of **2** is shown in Figure 1 (crystal data are summarized in Table S1, CCDC No. 2054549, 20544545, 2054548). The three complexes are isostructural, and therefore only **2** is described here as a representative of the other examples. The complex crystallized in the *Cc* space group, with eight $PhSAc^-$ ligands, two Pt ions, one Gd ion, one NEt_4 countercation, and two DMF crystalline solvents per asymmetry unit. The Gd ion forms a paddle-wheel-like structure with each Pt ion ($\{[Pt(PhSAc)_4]Gd[(PhSAc)_4Pt]\}^-$). The Gd ion is coordinated with eight O-atoms and two Pt ions to form a D_{4d} bicapped square antiprism geometry (Table S2). Each Pt ion is further coordinated with four sulfur atoms to form a square pyramidal structure with the Gd as the apex. The intramolecular Gd–Pt distances are 3.605(6) and 3.631(6) Å. These are shorter than the sum of the atomic radii (4.10 Å) but longer than the covalent (3.32 Å) and ionic (3.15 Å) radius[12] The first-sphere intermolecular Gd–Gd distances are 12.549(5), 14.264(6), and 14.62(6) Å.

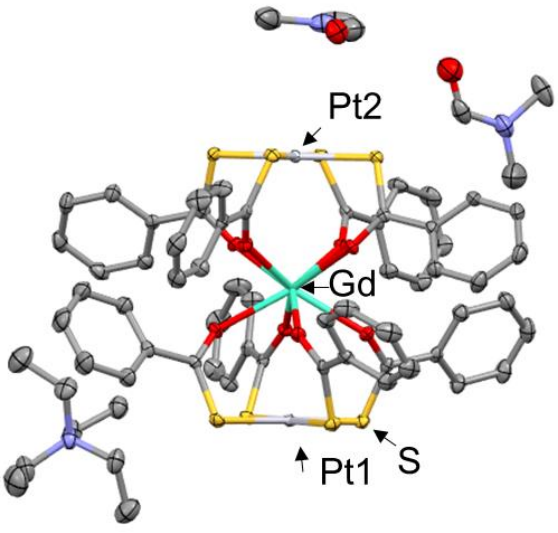

Figure 1. The crystal structure of **2**. White: Pt; Green: Gd; Pale purple: N; Grey: C; Yellow: S; Red: O. Hydrogen atoms have been omitted for clarity.

XANES analysis. Recently, several reports have revealed the covalency of Ln/An-ligand interactions involving the f-orbitals of metal complexes by using X-ray absorption.[13,14] The XANES spectra at the Pt L_3-edge are shown in Figure S1a. A white line shift from 11562.5 eV (peak top of the edge of the standard sample of Pt foil) to 11563.5 eV (for **1**), and 11563.4 eV (for **2**) was observed. The spectra were simulated by FDMNES package (Figure S1b-d).[15] and the results are similar to the XANES spectral features of tetrakis-m-pyrophosphitodiplatinate(II) ($[Pt_2(P_2O_5H_2)_4]^{4-}$) which has Pt–Pt bond.[16] In addition, we measured single-crystal polarized X-ray absorption spectra of **2** (Figure 2, beam size (< 100 μm) is small enough to *bc* plane of the crystal (200-300 μm per one side).) at different crystal axes with orientational information which allowed us to estimate the electronic state to estimate the electronic state of the metal centre.[17]

At the Pt L_{III}-edge, **2** showed that a weak white line (WL) absorption in the Pt–Ln–Pt direction (*c* direction: the direction perpendicular to Pt dx_2-y_2), but a strong WL absorption in the vertical direction (The results of density of states (DOS) calculation also supported the fact (Figure S1b,c)). On the other hand, at the Ln L_{III}-edge, contrast results were obtained. In **2**, the WL absorption is the strongest in the Pt−Ln−Pt (parallel) direction, but weak at the perpendicular direction as well as at 45 degrees from *c* axis. The 2p→5d transition is originally non-oriented (The results of DOS calculation also supported the fact (Figure S1d).), but the introduction of electrons into the 4f band shields the nuclear potential from the 5d band.[16] In other words, if the covalency between Ln and the ligand is high (or less ionic), the absorption intensity will increase. It can be said that the axial direction has higher covalency than the in-plane direction. Since the signal of the powder sample is an average of all orientations, the Pt direction has the highest covalency in **2**. Therefore, it was possible to experimentally clarify the anisotropy of the Ln complex's covalency in which it may be overall means ligand field splitting considering covalency

and electron repulsion, using the single-crystal polarized X-ray absorption spectrum. In this work, only the two-dimensional orientation is considered, and the LnPt molecule orientation (Pt–Ln–Pt direction) is also slightly leaning from *c* axis. Therefore, the comparison with the isotropic powder sample is not simple. However, further research will enable us to visualize the three-dimensional anisotropy of covalency.

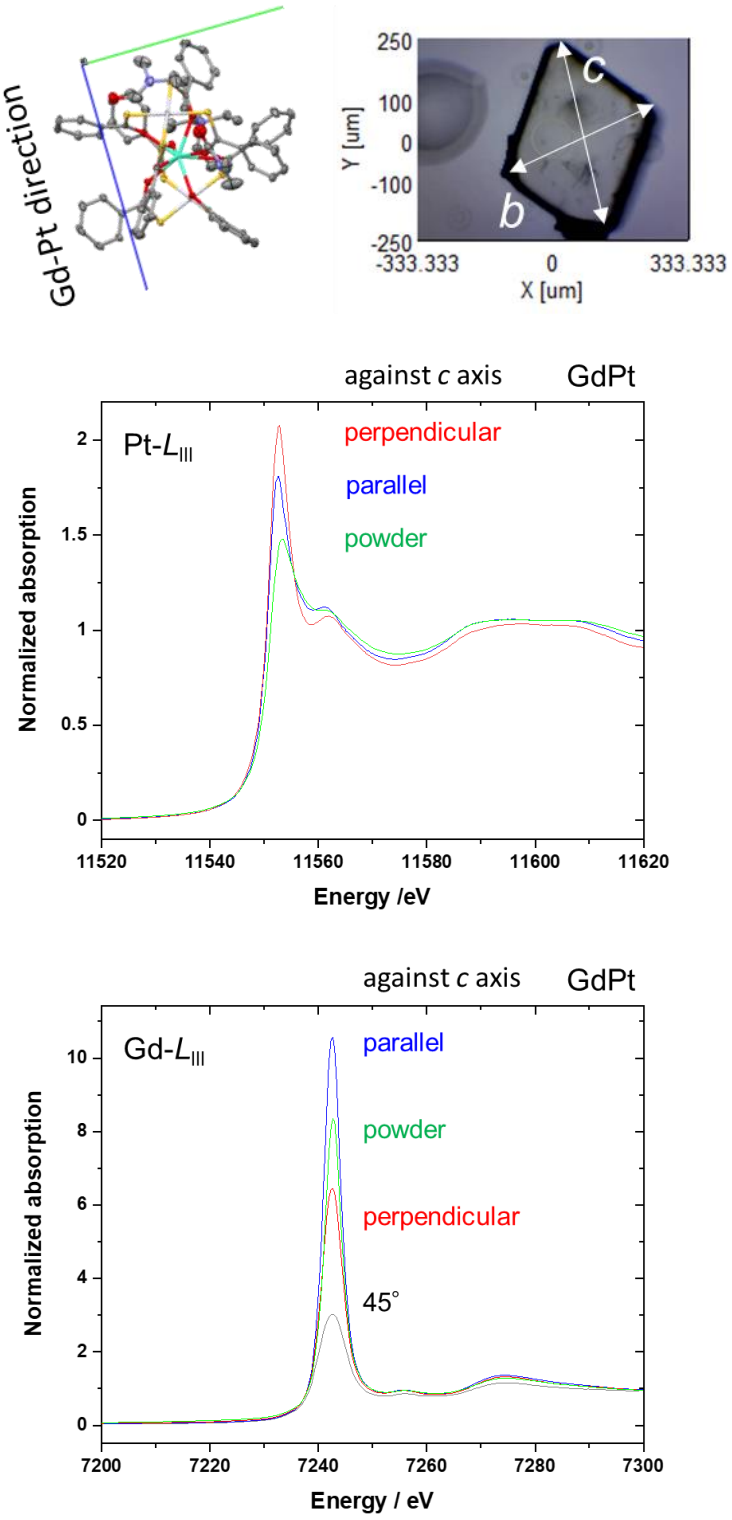

Figure 2. (a) A picture and orientation of a single crystal of **2**. Single-crystal polarized X-ray absorption spectra of **2**, (b)Pt-L_{III}; (c)Gd-L_{III}.

In the following sections, we examined the results of XANES or properties of Gd–Pt bond by clarifying donor-acceptor interaction, evaluation of bonds and electronic states.

NBO calculation. The natural bond orbital (NBO) analysis quantifies the donor-acceptor interactions between orbitals. The results of the NBO analysis using Gaussian16 program packages of **1** and **2** show the interactions between Ln and Pt ions (Table S3). There are strong Pt→La charge transfers in the range of ~36 kcal/mol. Moreover, there are several donor-acceptor Pt/Pt–S→La interactions in the range of 8−122 kcal/mol (threshold > 8 kcal/mol). On the other hand, **2** had weaker interactions than **1** did. (Table S4, 8−55 kcal/mol).

NPA calculation. The natural population analysis (NPA), which calculated atomic charge and orbital population for **1** and **2** using Gaussian16 program package, shows a charge transfer from the ligands to the Pt ion and Ln ion, from the Pt atoms to Ln ion (Table 1. If it is a free ion, an atomic charge of Ln ion is +3). The natural atomic charges of La, Pt, C_{Ac}, S, O, (per atom), and the sum per Ph group in **1** are around +1.464 −0.187, +0.380, +0.011, −0.648, and −0.006, respectively. In addition, the natural atomic charges of the Gd, Pt, C_{Ac}, S, O, (per atom), and Ph group are around +1.544, −0.209, +0.419, +0.003, −0.684, and −0.002, respectively, in **2**. The results of NBO and NPA is because the electron acceptability of Gd ion is lower than that of La ion (Details of the differences between Ln species are under investigation.).

Table 1. The natural atomic charges of La, Pt, C_{Ac}, S, O, $C_{Ph/Me}$ (per atom) for **1**, **2**

	La/Gd	Pt	C_{Ac}	S	O	Ph
1	+1.166	−0.235	+0.386	+0.083	−0.682	0.001
2	+1.723	−0.279	+0.380	+0.003	−0.725	~0.000

UV/vis spectra and TDDFT calculations. Experimental and calculated UV/Vis spectra of **2** are shown in Figure 3. Time-dependent density-functional theory (TDDFT) was used for calculating the absorption spectra. There are absorption peaks at 2.35, 3.32, and 4.20 eV for **2**. The peaks at 2.43 eV are almost absent for **0** and **1** (Figure S2a). The peaks for **2** have been assigned based on the results of the TDDFT calculation. The absorption at around 4.20 eV in the experimental spectra is attributed to DMF. However, we omitted the DMF molecule in the calculations to reduce the calculation cost. The peak observed at around 3.32 eV was assigned to the transition from the Pt-S molecular orbital to the Gd−O molecular orbital, and the peak around 2.35 eV was assigned to the transitions from the Pt–S molecular orbital to the Gd molecular orbitals (Figure S3). This Gd molecular orbital is an unoccupied orbital with 6s and 4f characters (s: 72.8%, p: 9.9% (mainly from the O atoms), d: 0.8%, f: 16.5%) (Figure 3c). The results of charge decomposition analysis (CDA) also indicated this hybridization (α orbital. Figure S4). The absorption peaks in the range 2.4 eV were also missing in previous reports ($[NEt_4][Gd\{Pt(SAc)_4\}_2]$, $[Gd_2Pt_3(SAc)_{12}]$ Figure. S2b),[10g, 10h,] confirming the d-f interaction in the excited state.

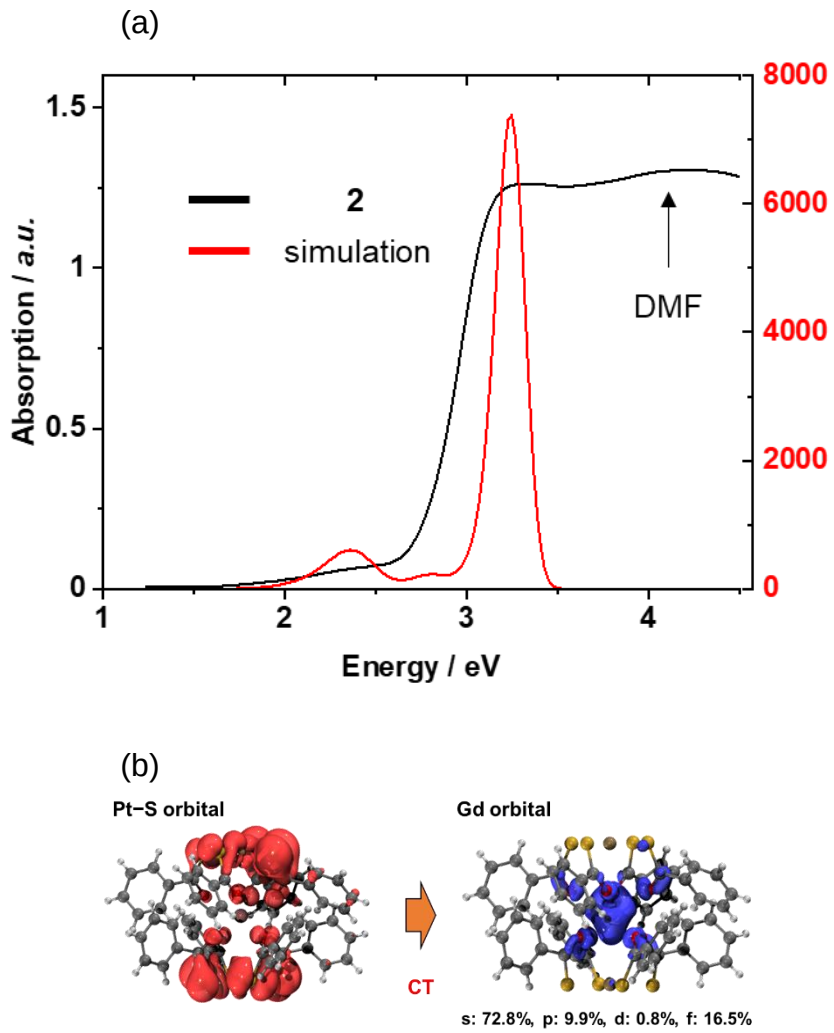

Figure 3. (a) Experimental and calculated UV/vis spectra of **2**, black: experimental; Red: calculation (DMF and counter cation have been omitted for the calculations). (b) Total composition Gd: 88.9%. Composition of each shell (%), the threshold of absolute value: greater than 0.50%: s: 72.8, p: 9.9, d: 0.8, f: 16.5 (p factor mainly coming from O atom).

Local orbital locator. The LOL is a method used to evaluate the bond between two atoms.[18a] If the LOL function is a simple sum of the LOL functions of each atom, the bond between the atoms is ionic. If a new peak exceeding 0.5 is observed between the two atoms, the bond between these atoms is covalent. A dative bond (footnote: Although it is labeled as polar covalent bond in the references,[18a] it is labeled as dative bond according to the AIM classification below.[18b]) will appear as a shoulder peak or as a plateau below 0.5. The LOL results for **2** show the existence of a shoulder, indicating that the Pt center was strongly polarized by the Ln center (Figure 4). These results may support the results of AIM. However, the LOL value ($\nu\sigma = 0.2$) is smaller than that obtained for the reported complexes (*cf.* $\nu\sigma = 0.3$); it means that the Gd−Pt bond in **2** is more ionic than that found for the reported complexes.[10b,10c]

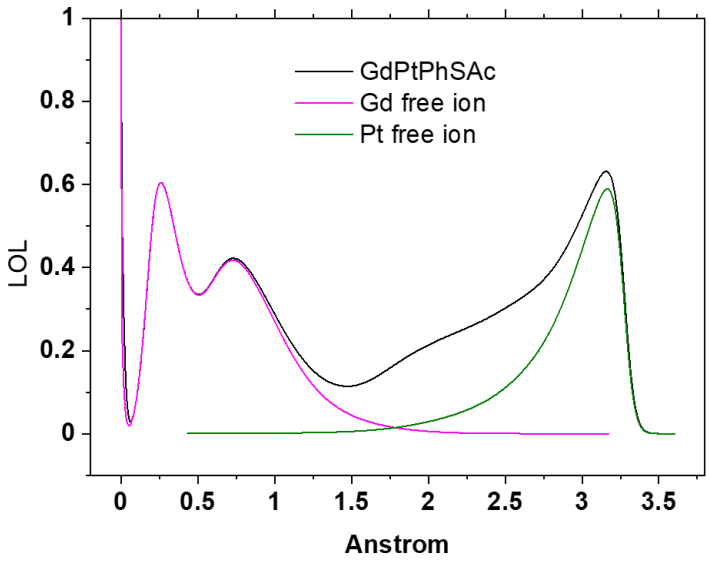

Figure 4. Local orbital locator plot between Pt and Gd.

Quantum theory of atoms in molecules analysis. Owing to quantum theory of atoms in molecules (QTAIM – see the experimental section for details of the calculation) analysis was performed to examine the electron density (ρ) of **1** and **2**. In QTAIM, there are usually three kinds of critical points where the differential of interatomic ρ is 0, so-called 'bond critical point (BCP)'. "Bond analysis using QTAIM requires the $\nabla^2\rho$ and E_{total} to have the following relationships - $\nabla^2\rho < 0$ and $E_{total} < 0$ signifies a covalent bond; $\nabla^2\rho > 0$ and $E_{total} < 0$ are values for dative bond; $\nabla^2\rho > 0$ and $E_{total} = \sim 0$ signal the existent of metallic bond while $\nabla^2\rho > 0$ and $E_{total} > 0$ indicate a possible ionic bond or Van der Waals force of attraction. (No bond has 100% covalency or 100% ionic. Even perfect covalent bond, which has 50% covalency and 50% ionic.)"[19] The contour plots on the Pt−Ln−Pt plane and the calculated value of ρ (electron density), and E_{total} (total energy density) were shown in Figure 5, S5, and Table 2. According to $\nabla^2\rho$ and E_{total} values, Ln−Pt bond is between metallic and ionic, whereas Pt−S bonds are dative. The covalency of Ln−Pt bond is lower than that of Ln−O bond. However, there is a possibility of underestimation of covalency of Ln−Pt bond (perhaps because of molecular packing) considering XAFS results. If the electron repulsion as well as the fact that $\rho_{Ln-Pt} < \rho_{Ln-O,}$ are considered, the AIM results are consistent with the XAFS results.

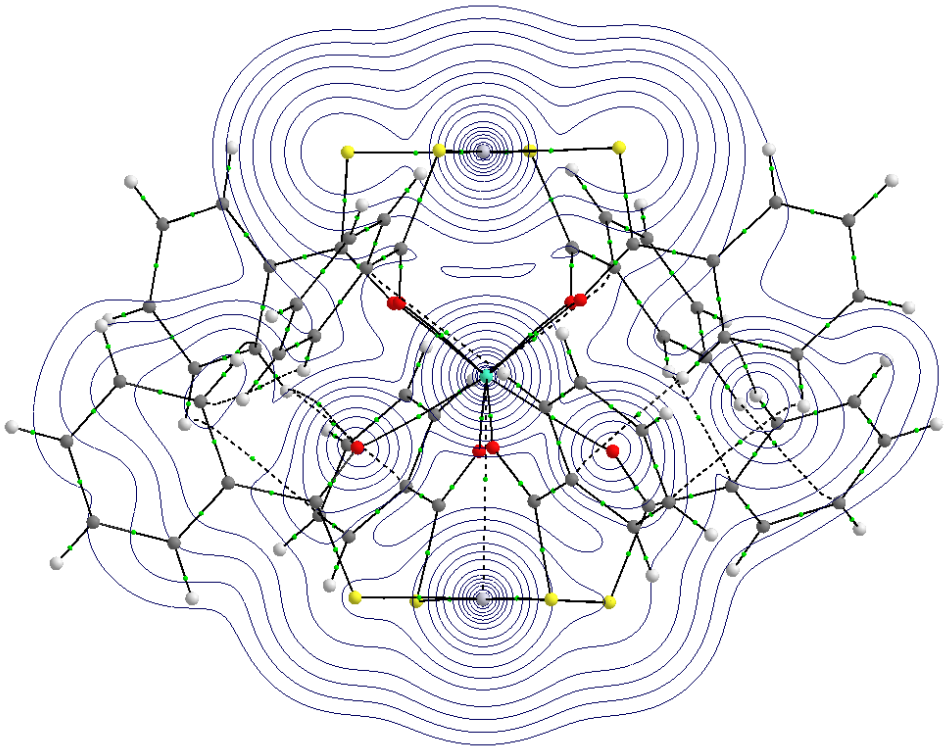

Figure 5. The contour plots on the Pt−Ln−Pt plane of **2**. Small green: BCP. White: Pt; Green: Gd; Grey: C; Yellow: S; Red: O.

Table 2. calculated QTAIM properties of **1** and **2**.

1	ρ	$\nabla^2\rho$	E_{total}	**2**	ρ	$\nabla^2\rho$	E_{total}
La - Pt1	0.00918	0.02807	0.00065	Gd1 - Pt1	0.00817	0.02759	0.00077
La - Pt1	0.01145	0.03178	0.00040				
La - O	0.04512	0.18285	0.00029	Gd - O	0.04709	0.21996	0.00088
	0.04536	0.18165	0.00005		0.04818	0.22580	0.00071
	0.04449	0.17790	0.00028		0.04793	0.22323	0.00060
	0.04536	0.18364	0.00022		0.04924	0.22965	0.00027
	0.04734	0.19202	-0.00020		0.04759	0.22249	0.00076
	0.04459	0.17753	0.00018		0.05017	0.23722	0.00033
	0.04613	0.18426	-0.00018		0.04819	0.22617	0.00070
	0.04451	0.17824	0.00034		0.04812	0.22651	0.00076
Pt1 - S	0.10742	0.14967	-0.04415	Pt1 - S	0.10928	0.15039	-0.04564
	0.10443	0.14554	-0.04182		0.10647	0.14806	-0.04342
	0.10728	0.14844	-0.04400		0.10749	0.15023	-0.04422
	0.10650	0.14836	-0.04342		0.10774	0.14895	-0.04441
Pt2 - S	0.10701	0.14792	-0.04381	Pt2 - S	0.10851	0.15031	-0.04502
	0.10622	0.14653	-0.04321		0.10535	0.14672	-0.04255
	0.10666	0.14785	-0.12404		0.10745	0.15050	-0.12601
	0.10824	0.14917	-0.12685		0.10763	0.14905	-0.12587

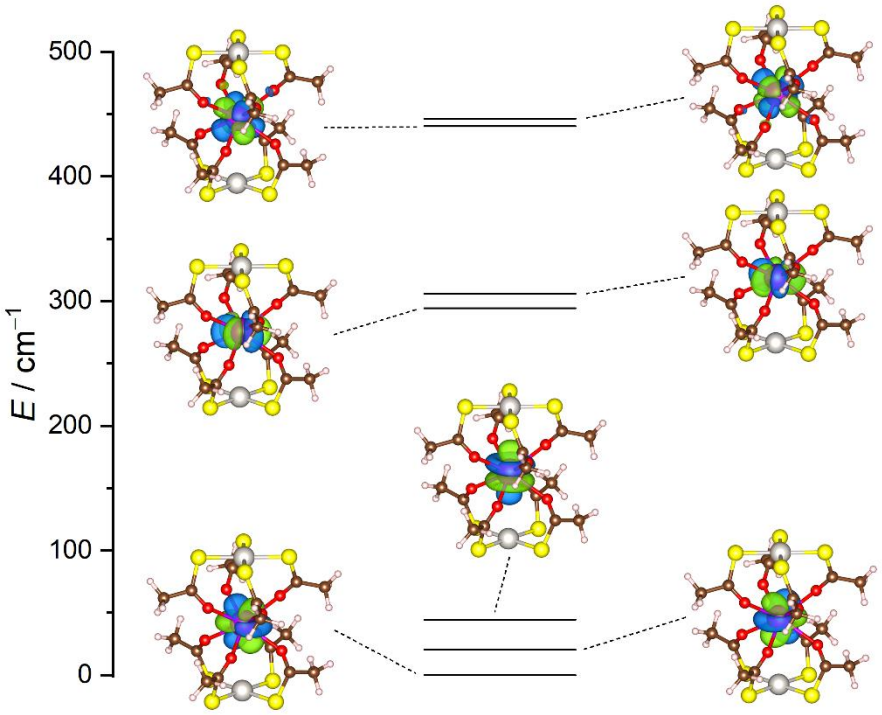

Figure 6. CASSCF ligand field orbitals of **2'-Me** obtained by ab initio ligand field theory.

As mention above, there are appreciable interactions among Gd and Pt ions. However, these interactions are polarizing and should not be considered as pure ionic or covalent (i.e. the Pt ion should not be treated as a positive point charge) under the ligand field theory of the Gd ion.

Ab initio calculations were performed using the ORCA 4.2.1 program.[20] The active space consists of 7 electrons in 7 orbitals (CASSCF(7,7)). For the state-averaged CASSCF procedure, 1 octet, 48 sextets, 392 quartets, and 784 doublets were considered[21] for the configuration state functions (CSFs) and used for the spin-orbit coupling calculations. The low-lying energy states from spin-orbit coupling are summarized in Table 3. *Ab initio* ligand field theory (AILFT)[11b] was applied to check the ligand field splitting of 4f-orbitals of **2'-Me** (Figure 6). The results showed a ligand field splitting energy of ~450 cm^{-1}. In terms of orbital stability, the axial (Pt-Gd-Pt direction) fz^3, fxz^2 and fyz^2 orbitals are most stabilized, the equatorial $fx(x^2-3y^2)$ and $fy(3x^2-y^2)$ orbitals are intermediate while the diagonal fxyz, $fz(x^2-y^2)$ orbitals are the least stabilized. This order (axial, equatorial, diagonal) is similar to the results of the single-crystal XAFS – less ionic orientation order (parallel, perpendicular, 45 degrees). In addition, fz^3 orbital is less stable than fxz^2, fyz^2 orbital, because fz^3 orbital also undergoes electrostatic repulsion from the lone pair of the Pt ion.

Table 3. Wavefunction composition and energy levels of the low-lying spin-orbit states of **2'-Me** obtained by CASSCF calculations. Theses energy levels correspond to the zero-field splitting of $^8S_{7/2}$ state. Wavefunction compositions are given using $|J_z>$ states of $^8S_{7/2}$ as the basis functions. Zero-field splitting parameters are given in spin Hamiltonian formalism.

Composition of the wavefunction	*Energy*/cm^{-1}
0.967|−1/2>	0.000
0.967|+1/2>	0.000
0.327|+3/2>, 0.637|−3/2>	0.0763
0.637|+3/2>, 0.327|−3/2>	0.0763
0.107|+5/2>, 0.866|−5/2>	0.2228
0.866|+5/2>, 0.107|−5/2>	0.2228
0.978|−7/2>	0.4347
0.978|+7/2>	0.4347
Zero-field splitting parameters	
D/cm^{-1}	0.03612
E/*D*	0.02245

Magnetic properties. Recently, several studies on the slow magnetic relaxation of Gd complexes have been reported.[22] Although the decisive relaxation mechanism for Gd complex has not been elucidated yet, it has been assumed that magnetic relaxations of Gd complexes are driven by various kinds of relaxation mechanisms: phonon-bottleneck process, Orbach process, direct process, and Raman process.[22a,22b] Moreover, magnetic relaxations are affected by magnetic dilution. Increasing the concentration of Gd ion increases the internal magnetic field, enhancing the magnetic relaxations. On the other hand, high Gd concentration prohibits rapid energy exchange and enhances the phonon-bottleneck effect because phonon modes available for spin-lattice relaxations are saturated.

Yamashita et al. and Pinkowicz et al. have reported slow magnetic relaxation for mononuclear Gd complexes.[23] However, the spin-lattice relaxation is only observed below 10 K, which is a much lower temperature range than the 36 K observed for heterometal complexes.[10g] For **2**$_{0.1}$, a slow magnetic relaxation was observed up to 45 K (Figure 8b). This is the highest temperature reported to date for a discrete Gd complexes.

$\chi_m T$ values for **2** and **2**$_{0.1}$(10% of **2** diluted in 90 % of **0**) remained constant at 8.168 cm^3 mol^{-1} K and 7.872 cm^3 mol^{-1} K, respectively, which are consistent with the expected value for an uncoupled Gd ion (7.875 cm^3 mol^{-1} K) (Figure 8a and S6). Moreover, **2** and **2**$_{0.1}$ did not exhibit a magnetic ordering down to 2 K. The magnetization *vs*. field plots for **2** and **2**$_{0.1}$ are shown in Figure. S7. There is butterfly-type hysteresis for **2** and **2**$_{0.1}$ at 1.8 K, indicating a rapid quantum tunnelling effect. The hysteresis temperature is higher than those reported for Gd complexes (cf. 0.7 K).[10g]

No clear frequency dependence of the magnetization was observed for **2** without a *dc* field because of the fast QTM (the quantum tunnelling of the magnetization) process. However, **2** shows

the explicit frequency dependency of the magnetization with applied *dc* field was applied (Figure S8). Furthermore, as the dc field was gradually increased, the maximum χ" shifted to a lower frequency, and an additional peak was observed above 4000 Oe *dc* fields. This second peak was not observed for **2$_{0.1}$** (Figure S9). Yamashita *et al.* reported a similar phenomenon as a phonon-bottleneck. In-phase and out-of-phase data for **2$_{0.1}$** were fitted to extract the relaxation time τ using the extended Debye model (details are shown in the ESI). The relaxation time was fitted by considering the direct, Raman, and Orbach processes using the equation:[22b] $\tau^{-1}(\mathrm{H}) = A_1/(1 + A_2H^2) + A_3H^4 + A_4$ and with A_1: 600 s^{-1}, A_2: 1.48 Oe^{-2}, A_3: 0.81 Oe^{-4}, A_4: 191 s^{-1}, R = 0.99959.

The temperature dependence of the *ac* susceptibility of **2$_{0.1}$** up to 45 K in a 3000 Oe *dc* field is shown in Figure 8b. In-phase and out-of-phase data for **2$_{0.1}$** were fitted to extract τ values using the extended Debye model (Figure 8c). The relaxation time was fitted by considering the direct, Raman, and Orbach processes using the equation: $\ln \tau(T^{-1}) = \ln[(C_1T + C_2T^n) + \tau_0\exp(-E/T))^{-1}] + A_4$ with $A_3H^4 = C_1T$, C_2: 10.25 s^{-1}, n: 2.52, τ_0: 2.2 × 10^{-3} s, E: 1.52 K, R = 0.99895. Fittings were performed on this data under various conditions. In conclusion, the process involving both the Orbach and two-phonon Raman ($\tau \propto 1/T^3$) processes afforded the best fit (Figure S10). Low-energy phonon modes (15-60 cm^{-1}) that may resonate with the magnetic Raman process have been experimentally observed, and DFT calculations have revealed that they correspond to the PtS_4−LnO_8−PtS_4 oscillation modes (Figure S12, S13. The Raman spectra discuss in SI.). The smaller resonant phonon mode that resonates with the Orbach process is thought to be caused by the lattice vibration of the crystal packing (Figure S11).

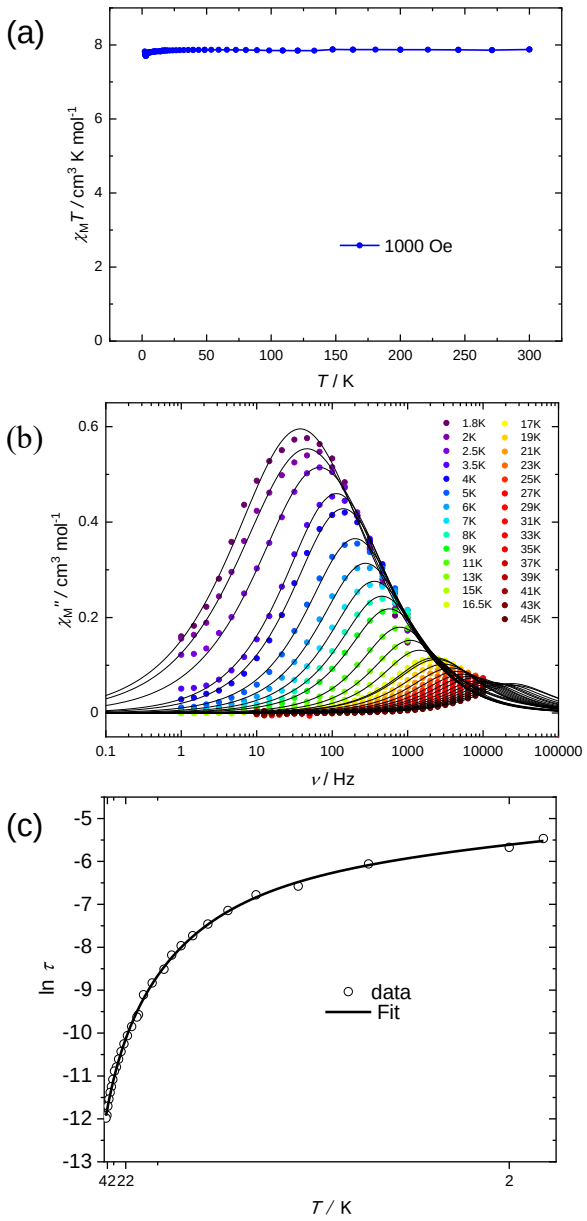

Figure 8. (a) χ_MT *vs*. *T* plots for **2$_{0.1}$** in a field of 1000 Oe. (b) χ''_M *vs*. *T* plots for **2$_{0.1}$** in a field of 3000 Oe and the *T* range of 1.8–45 K. (c) ln(τ) vs. T^{-1} plots for **2$_{0.1}$**.

To investigate the zero-field splitting of Gd ion, we measured ESR spectrum of **2**$_{0.05}$ (5% of **2** diluted in 95 % of **0**) (Figure. 7 and S17). The data were fitted using the Hamiltonian $\hat{\mathrm{H}} = \mu_B B\hat{S} + B_2^0\hat{O}_2^0 + B_2^2\hat{O}_2^2$ (Details are shown in SI.) with EasySpin package.[23] The parameters were fitted as $B_2^0 = 317.8$ MHz = 1/3*D*, $B_2^2 = -52.8$ MHz = *E*, *g* = (1.986, 1.982 1.866), *A* = 15.6 MHz, lw = 4.9 mT, respectively. The B_2^0 (1/3*D)* value was obtained as 318 MHz, which is smaller than the reported value, B_2^0 (1/3*D)* = 554.7 MHz[24](*D*: axial zero-field splitting value, *E*: rhombic zero-field splitting value, *A*: hyperfine principal value, lw: Gaussian broadening). There are some differences between the experimental and the simulated values, owing to the approximations used during simulations.[10h,21] These are inevitable to avoid overparameterization.[25] Wavefunction composition and energy levels of the low-lying spin-orbit states of **2'-Me** were obtained by CASSCF calculations (Table 3). These energy levels correspond to the zero-field splitting of $^8S_{7/2}$ state. The calculated zero-field splitting parameter *D* (0.03612 cm^{-1} = 1082 MHz), *E*/*D* (0.02245) is consistent with that fitting value of results of ESR (*D* = 953.4 MHz, 0.05538).

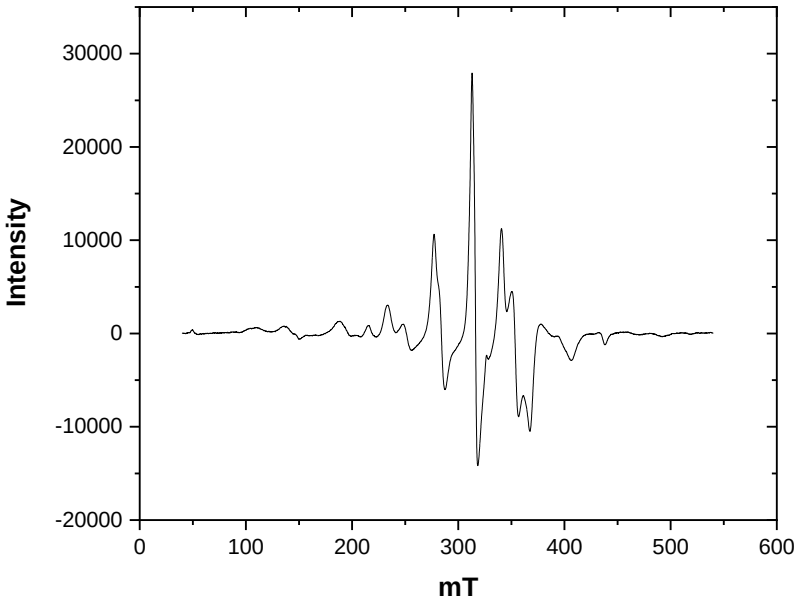

Figure 7. ESR spectrum of $\mathbf{2}_{\mathbf{0.05}}$(5% of **2** diluted in 95 % of **0**).

CONCULUSION

We provided the insight into the Gd–Pt bond by calculating NPA and AIM and revealed the electronic states using X-ray absorption near edge structure (XANES). These calculations will enable the role of metallic and organic ligands in the electronic and magnetic properties of Ln complexes to be further understood. The slow magnetization relaxation of the Gd complex was observed up to 45K, which is the highest temperature reported to date among isolated Gd-complexes. In such a metallic ligand system, it is necessary to calculate the electronic state considering the influence of the orbital of the metal ion instead of treating the metal ion as a mere positive point charge. Further careful consideration for the effect of the heterometal bonds such as the complexes with higher covalency is required when discussing the magnetic properties of heterometallic bonded systems.

Experimental Section

General information. $K_2[PtCl_4]$ was obtained from Kanto Chemical Co., Inc. and used as received. $LnCl_3 \cdot nH_2O$ was obtained from Strem Chemicals Inc. and used as received. Thiobenzoic acid ((PhSAc)H) was obtained from Tokyo Chemical Industry Co., Ltd. and used as received. All synthetic processes were performed under air.

Synthesis of 0, 1, and 2. The aqueous solution (5 ml) of $K_2[PtCl_4]$ (50 mg: 0.125 mmol) and $LnCl_3 \cdot nH_2O$ (Ln = Y, La, Gd; 13, 23 mg: 0.062 mmol) was added to a DMF solution (15 ml) of 70 mg (0.5 mmol) (PhSAc)H and tetraethylammonium chloride (10 mg: 0.061 mmol). The solution was stirred at 60 °C for 2 h. After evaporation, the resulting solid was dissolved in DMF, and KCl was removed by filtration. A yellow crystal was obtained after slow evaporation under flowing N_2 (Scheme 1. yield: ~43%, ~50 mg).

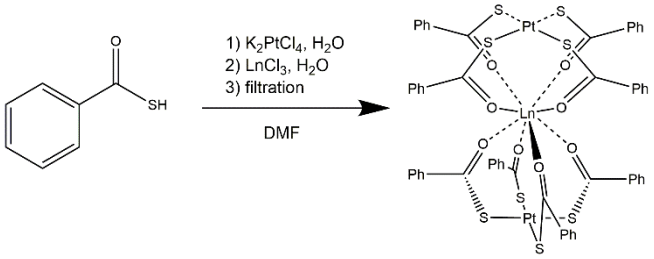

Scheme 1. Synthesis of **0**, **1**, and **2**.

$[YPt_2(PhSAc)_8](NEt_4) \cdot 2DMF$ (0)

Elemental analysis: $C_{70}H_{74}N_3O_{10}S_8Pt_2Y$; Calcd(%): C, 45.38; H, 4.03; N, 2.27. Found(%); C, 45.41; H, 4.13; N, 2.29. IR spectrum (ATR, cm^{-1}): 3055, 2928, 2847, 1675, 1583, 1530, 1476, 1444, 1385, 1307, 1208 1169, 1086, 1000, 945, 866, 773, 688, 647, 617.

[$LaPt_2(PhSAc)_8$](NEt_4)· 2DMF (1)

Elemental analysis: $C_{70}H_{74}N_3O_{10}S_8Pt_2La$; Calcd(%): C, 44.18; H, 3.92; N, 2.21. Found(%); C, 44.22; H, 3.97; N, 2.43. IR spectrum (ATR, cm^{-1}): 3057, 2938, 2850, 1670, 1583, 1527, 1484, 1443, 1386, 1314, 1206 1169, 1092, 999, 944, 869, 772, 688, 647, 617.

[$GdPt_2(PhSAc)_8$](NEt_4)· 2DMF (2)

Elemental analysis: $C_{70}H_{74}N_3O_{10}S_8Pt_2Gd$; Calcd(%): C, 43.76; H, 3.88; N, 2.19. Found(%); C, 43.64; H, 3.90; N, 2.36. IR spectrum (ATR, cm^{-1}): 3057, 2938, 2850, 1676, 1581, 1522, 1474, 1445, 1386, 1314, 1202 1173, 1083, 1006, 941, 864, 775, 686, 639, 568.

Characterization and instrumental procedures. Single-crystal X-ray diffraction data were collected on a Rigaku VariMax diffractometer with a HyPix-6000 detector (details of of crystallographic data collection described on CIF files). FT-IR spectra were acquired on a JASCO FT/IR 6700 spectrometer using the attenuated total reflectance (ATR) method. UV/vis spectra were acquired on a Shimadzu UV3100 spectrometer with an integrating sphere ($BaSO_4$ background). The elemental analysis was performed on a J-SCIENCE LAB CO., Ltd JM-11 microanalyzer. The Raman spectra were carried out on a JASCO NRS-7200.

Calculations. TDDFT, NBO, NPA, LOL, simulation of Raman spectra analyses were performed using the Gaussian16 program package. Quantum theory of atoms in molecules (QTAIM) analysis was performed in the AIMAll package.[26] The molecular structure of the model is made from the crystal structure of **1**, **2** and simplified using GaussView5.0. The B3LYP functional[27] was used with Def2-SVP (for C, H),[28a] Def2-TZVP (for S, O),[28a] Def2-TZVPD (for Pt)[28a] with ECP,[28b] Stuttgart quadruple zeta split + RSC Segmented (for Gd)[28c] with ECP[28d] for the LOL, TDDFT

calculations and simulation of Raman spectra; with aug-cc-pCVDZ-DK (for C, H, S, O),[28e-h] Sapporo-DKH3-TZP-2012 (for Pt),[28i] SARC2-QZV-DKH2 (for Gd)[28j] for NBO, NPA, AIM under Douglas-Kroll-Hess option.

Ab initio calculations were performed using the ORCA 4.2.1 program.[20] The structural model (**2'-Me**) used for ab initio calculations was made by replacing phenyl groups of the crystal coordinate of **2** with methyl groups (Table S6). Positions of the methyl protons of **2'-Me** were optimized at B3LYP/Def2-SVP with the RIJCOSX approximation. During the geometry optimization, Gd was replaced with diamagnetic Y. The CASSCF method was applied to **2'-Me** with DKH-DEF2-SVP (for C, H, S, O), SARC-DKH-TZVP (for Pt), SARC-DKH-TZVPP (for Gd).[28b] AUTOAUX keyword[29] was used to generate the auxiliary basis sets for resolution of identity approximation.[30] The active space consists of the seven orbitals that have 4f character and seven electrons ((7,7) CASSCF). One octet state, 48 sextet states, 392 quartet states, and 784 doublet states were considered[21] and used for the following spin-orbit coupling calculations. The low-lying energy states from spin-orbit coupling are summarized in Table S8. Ab initio ligand field theory (AILFT)[11b] was applied to check the ligand field splitting of 4f-orbitals (Figure S11). Orbitals were visualized using Multiwfn 3.7 and VESTA 3.4.4.[31] The coordination geometry as determined using SHAPE2.1.[32]

Charge decomposition analysis (CDA) is one of the methods to analyze donor-acceptor interactions of each fragment of complexes.[33] Here, We took complex **2** to three parts: Gd ion, Pt ions, and PhSAc ligands. CDA was performed on Multiwfn 3.7.[31a]

X-ray absorption near-edge structure. X-ray absorption spectroscopy was carried out at the BL-12C and BL9A, High Energy Accelerator Research Organization (KEK) (the edge position was

calibrated using that of Pt foil). The analysis was performed using the Demeter software platform.[34] The simulated spectra are calculated with 6 Å radius by FDMNES package under Quadrupole, Relativiste, Spinorbite, Density_all options.[18]

Magnetic susceptibility measurements. Both *dc* and *ac* magnetic susceptibility measurements were performed on solid polycrystalline samples with a Quantum Design MPMS3 SQUID magnetometer in applied *dc* fields. ESR spectra were conducted on solid polycrystalline samples using a JEOL JES-FA100.

ASSOCIATED CONTENT

Supporting Information.

The following files are available free of charge.

Some additional figure and plots.

Author Contributions

Authors may have contributed in multiple roles.

Notes

The authors declare no competing financial interests.

ACKNOWLEDGMENT

This research was supported by JSPS KAKENHI Grant Numbers JP19H05631 (HI, ST, and MY), JP19H02729 (ST), JP20K15293 (TY). Prof. M. Yamashita acknowledges the support of the 111 projects (B18030) from China. The Raman spectra were carried out in the Analysis and Instrumentation Center, Nagaoka University of Technology. The computation was carried out using the computer resource offered under the category of Trial Use Projects by Research Institute

for Information Technology, Kyushu University. Part of the experimental results in this research were obtained using supercomputing resources at Cyberscience Center, Tohoku University. This work was performed under the approval of the Photon Factory Program Advisory Committee (Proposal No. 2019G117, beamline 12C, 9A).

REFERENCES

(1) a) Jin, P.-B.; Zhai, Y.-Q.; Yu, K.-X.; Winpenny, R. E. P.; Zheng, Y.-Z., Dysprosiacarboranes as Organometallic Single-Molecule Magnets. *Angew. Chem. Int. Ed.*, **2020**, *59*, 9350-9354; b) Errulat, D.; Gabidullin, B.; Mansikkamäki, A.; Murugesu, M., Two heads are better than one: improving magnetic relaxation in the dysprosium metallocene upon dimerization by use of an exceptionally weakly-coordinating anion. *Chem. Commun.*, **2020**, *56*, 5937-5940; c) Durrant, J. P.; Tang, J.; Mansikkamäki, A.; Layfield, R. A., Enhanced single-molecule magnetism in dysprosium complexes of a pristine cyclobutadienyl ligand. *Chem. Commun.*, **2020**, *56*, 4708-4711; d) Ling, B.-K.; Zhai, Y.-Q.; Han, J.; Han, T.; Zheng, Y.-Z., A stable dysprosium(iii) complex with a terminal fluoride ligand showing high resolution luminescence and slow magnetic relaxation. *Dalton Trans.*, **2020**, *49*, 6969-6973; e) Li, M.; Wu, H.; Xia, Z.; Ungur, L.; Liu, D.; Chibotaru, L. F.; Ke, H.; Chen, S.; Gao, S., An Inconspicuous Six-Coordinate Neutral DyIII Single-Ion Magnet with Remarkable Magnetic Anisotropy and Stability. *Inorg. Chem.*, **2020**, *59*, 7158–7166; f) Lemes, M. A.; Mavragani, N.; Richardson, P.; Zhang, Y.; Gabidullin, B.; Brusso, J. L.; Moilanen, J. O.; Murugesu, M., Unprecedented intramolecular pancake bonding in a {Dy_2} single-molecule magnet. *Inorg. Chem. Front.*, **2020**, *7*, 2592-2601; g) Velkos, G.; Yang, W.; Yao, Y.-R.; Sudarkova, S. M.; Liu, X.; Büchner, B.; Avdoshenko, S. M.; Chen, N.; Popov, A. A., Shape-adaptive single-molecule magnetism and hysteresis up to 14 K in oxide clusterfullerenes $Dy_2O@C_{72}$ and $Dy_2O@C_{74}$ with fused pentagon pairs and flexible Dy–(μ_2-O)–Dy angle. *Chem. Sci.*, **2020**, *11*, 4766-4772; h) Vignesh, K. R.; Alexandropoulos, D. I.; Xie, H.; Dunbar, K. R., Six-coordinate mononuclear dysprosium(iii) single-molecule magnets with the triphenylphosphine oxide

ligand. *Dalton Trans.*, **2020**, *49*, 4694-4698; i) Goodwin, C. A. P.; Réant, B. L. L.; Vettese, G. F.; Kragskow, J. G. C.; Giansiracusa, M. J.; DiMucci, I. M.; Lancaster, K. M.; Mills, D. P.; Sproules, S., Heteroleptic Samarium(III) Chalcogenide Complexes: Opportunities for Giant Exchange Coupling in Bridging σ- and π-Radical Lanthanide Dichalcogenides. *Inorg. Chem.*, **2020**, *59*, 7571–7583; j) Izuogu, D. C.; Yoshida, T.; Cosquer, G.; Asegbeloyin, J. N.; Zhang, H.; Thom, A. J. W.; Yamashita, M., Periodicity of Single‐Molecule Magnet Behaviour of Heterotetranuclear Lanthanide Complexes Across the Lanthanide Series: A Compendium. *Chem. Eur. J.*, **2020**, *26*, 6036-6049; k) Leng, J.-D.; Hua, Q.-Y.; Lin, L.-S.; Lin, W.-Q.; Liu, J.-L.; Pan, Y.-Z.; Qiu, Y.-B.; Zhou, A.-J., A slowly magnetic relaxing SmIII monomer with a D5h equatorial compressed ligand field. *Inorg. Chem. Front.*, **2020**, *7*, 2335-2342; l) Latendresse, T. P.; Vieru, V.; Upadhyay, A.; Bhuvanesh, N. S.; Chibotaru, L. F.; Nippe, M., Trends in trigonal prismatic Ln-[1]ferrocenophane complexes and discovery of a Ho3+ single-molecule magnet. *Chem. Sci.*, 2020, **11**, 3936-3951; (m) Yamashita, M. B*ull, Chem. Soc. Jpn.*, **2021**, *94*, 209-264.

(2) a) Ayers, K. M.; Schley, N. D.; Ung, G., Circularly Polarized Luminescence from Enantiopure C2-Symmetrical Tetrakis(2-pyridylmethyl)-1,2-diaminocyclohexane Lanthanide Complexes. *Inorg. Chem.*, **2020**, DOI: 10.1021/acs.inorgchem.0c00628; b) Kofod, N.; Nawrocki, P.; Juelsholt, M.; Christiansen, T. L.; Jensen, K. M. Ø.; Sørensen, T. J., Solution Structure, Electronic Energy Levels, and Photophysical Properties of $[Eu(MeOH)_{n-2m}(NO3)_m]^{3-m+}$ Complexes. *Inorg. Chem.*, **2020**, DOI: 10.1021/acs.inorgchem.0c00056; c) Kamebuchi, H.; Yoshioka, T.; Tadokoro, M., Development of tuneable green-to-red emitting transparent film based on Nafion with TbIII/EuIII β-diketonate complexes modulated by pH and proton flow. *Materials Advances*, **2020**, *1*, 569-573; d) Yang, Z.-S.; Yao, Y.; Sedgwick, A. C.; Li, C.; Xia, Y.; Wang, Y.; Kang, L.; Su, H.; Wang, B.-W.; Gao, S.; Sessler, J. L.; Zhang, J.-L., Rational design of an "all-in-one" phototheranostic. *Chem. Sci.*, **2020**, DOI: 10.1039/D0SC03368E; e) Kovacs, D.; Mathieu, E.; Kiraev, S. R.; Wells, J. A. L.; Demeyere, E.; Sipos, A.; Borbas, K. E., Coordination Environment-Controlled Photoinduced Electron Transfer Quenching in Luminescent Europium Complexes. *J. Am. Chem. Soc.*, **2020**, *142*, 13190-13200; f) Knighton, R. C.; Soro, L. K.; Lecointre, A.; Pilet, G.; Fateeva, A.; Pontille, L.; Francés-

Soriano, L.; Hildebrandt, N.; Charbonnière, L. J., Upconversion in molecular hetero-nonanuclear lanthanide complexes in solution. *Chem. Commun.*, **2021**, DOI: 10.1039/D0CC07337G.

(3) a) Ramirez, B. L.; Lu, C. C., Rare-Earth Supported Nickel Catalysts for Alkyne Semihydrogenation: Chemo- and Regioselectivity Impacted by the Lewis Acidity and Size of the Support. *J. Am. Chem. Soc.*, **2020**, *142*, 5396-5407; b) Ramirez, B. L.; Sharma, P.; Eisenhart, R. J.; Gagliardi, L.; Lu, C. C., Bimetallic nickel-lutetium complexes: tuning the properties and catalytic hydrogenation activity of the Ni site by varying the Lu coordination environment. *Chem. Sci.*, **2019**, *10*, 3375-3384; c) Halter, D. P.; Palumbo, C. T.; Ziller, J. W.; Gembicky, M.; Rheingold, A. L.; Evans, W. J.; Meyer, K., Electrocatalytic H2O Reduction with f-Elements: Mechanistic Insight and Overpotential Tuning in a Series of Lanthanide Complexes. *J. Am. Chem. Soc.*, **2018**, *140*, 2587–2594.

(4) Guo, F.-S.; Day, B. M.; Chen, Y.-C.; Tong, M.-L.; Mansikkamäki, A.; Layfield, R. A., A Dysprosium Metallocene Single-Molecule Magnet Functioning at the Axial Limit. *Angew. Chem. Int. Ed.*, **2017**, *56*, 11445-11449.

(5) Goodwin, C. A. P.; Ortu, F.; Reta, D.; Chilton, N. F.; Mills, D. P., Molecular magnetic hysteresis at 60 kelvin in dysprosocenium. *Nature*, **2017**, *548*, 439-442.

(6) a) Kuga, K.; Kanai, Y.; Fujiwara, H.; Yamagami, K.; Hamamoto, S.; Aoyama, Y.; Sekiyama, A.; Higashiya, A.; Kadono, T.; Imada, S.; Yamasaki, A.; Tanaka, A.; Tamasaku, K.; Yabashi, M.; Ishikawa, T.; Nakatsuji, S.; Kiss, T., Effect of Anisotropic Hybridization in $YbAlB_4$ Probed by Linear Dichroism in Core-Level Hard X-Ray Photoemission Spectroscopy. *Phys. Rev. Lett.*, **2019**, *123*, 036404; b) Sasabe, N.; Tonai, H.; Uozumi, T., Spectral Change in 3d–4f Resonant Inelastic X-ray Scattering of Ce Intermetallics Across the Transition between Kondo Singlet and Localized-Spin State. *J. Phys. Soc. Jpn.*, **2017**, *86*, 093701; c) Okawa, M.; Matsunami, M.; Ishizaka, K.; Eguchi, R.; Taguchi, M.; Chainani, A.; Takata, Y.; Yabashi, M.; Tamasaku, K.; Nishino, Y.; Ishikawa, T.; Kuga, K.; Horie, N.; Nakatsuji, S.; Shin, S., Strong Valence Fluctuation in the Quantum Critical Heavy Fermion Superconductor β-$YbAlB_4$: A Hard X-Ray Photoemission Study. *Phys. Rev. Lett.*, **2010**, *104*, 247201; d) Mathur, N. D.; Grosche, F. M.; Julian, S. R.; Walker, I.

R.; Freye, D. M.; Haselwimmer, R. K. W.; Lonzarich, G. G., Magnetically mediated superconductivity in heavy fermion compounds. *Nature*, **1998**, *394*, 39-43; e) Miyake, K.; Schmitt-Rink, S.; Varma, C. M., Spin-fluctuation-mediated even-parity pairing in heavy-fermion superconductors. *Phys. Rev. B*, **1986**, *34*, 6554-6556; f) Scalapino, D. J.; Loh, E.; Hirsch, J. E., d-wave pairing near a spin-density-wave instability. *Phys. Rev. B*, **1986**, *34*, 8190-8192.

(7) Rice, N. T.; Popov, I. A.; Russo, D. R.; Bacsa, J.; Batista, E. R.; Yang, P.; Telser, J.; La Pierre, H. S., Design, Isolation, and Spectroscopic Analysis of a Tetravalent Terbium Complex. *J. Am. Chem. Soc.*, **2019**, *141*, 13222-13233.

(8) a) Hu, S.-X.; Lu, E.; Liddle, S. T., Prediction of high bond-order metal–metal multiple-bonds in heterobimetallic 3d–4f/5f complexes [TM–M{N(o-[$NCH_2P(CH_3)_2$]C_6H_4)$_3$}] (TM = Cr, Mn, Fe; M = U, Np, Pu, and Nd). *Dalton Trans.*, **2019**, *48*, 12867-12879; b)A. Ayres, A. J.; Zegke, M.; Ostrowski, J. P. A.; Tuna, F.; McInnes, E. J. L.; Wooles, A. J.; Liddle, S. T., Actinide-transition metal bonding in heterobimetallic uranium– and thorium–molybdenum paddlewheel complexes. *Chem. Commun.*, **2018**, *54*, 13515-13518; c) Lu, E.; Wooles, A. J.; Gregson, M.; Cobb, P. J.; Liddle, S. T., A Very Short Uranium(IV)‐Rhodium(I) Bond with Net Double‐Dative Bonding Character. *Angew. Chem. Int. Ed.*, **2018**, *57*, 6587-6591. d) Yang, X.; Burns, C. P.; Nippe, M.; Hall, M. B., Unsupported Lanthanide–Transition Metal Bonds: Ionic vs Polar Covalent? *Inorg. Chem.* **2021,** *60*, 9394–9401.

(9) Briganti, M.; Garcia, G. F.; Jung, J.; Sessoli, R.; Guennic B. Le; and Totti, F. Covalency and magnetic anisotropy in lanthanide single molecule magnets: the DyDOTA archetype. *Chem. Sci.*, **2019**, *10*, 7233-7245.

(10) a) Bonde, N. A.; Petersen, J. B.; Sørensen, M. A.; Nielsen, U. G.; Fåk, B.; Rols, S.; Ollivier, J.; Weihe, H.; Bendix, J.; Perfetti, M., Importance of Axial Symmetry in Elucidating Lanthanide–Transition Metal Interactions. *Inorg. Chem.*, **2019**, *59*, 235-243; b) Yoshida, T.; Izuogu, D. C.; Zhang, H.; Cosquer, G.; Abe, H.; Wernsdorfer, W.; Breedlove, B. K.; Yamashita, M., Ln-Pt Electron Polarization Effects on the Magnetic Relaxation of Heterometallic Ho- and Er-Pt Complexes. *Dalton Trans.*, **2019**, *48*, 7144-

7149; c) Izuogu, D. C.; Yoshida, T.; Zhang, H.; Cosquer, G.; Katoh, K.; Ogata, S.; Hasegawa, M.; Nojiri, H.; Damjanović, M.; Wernsdorfer, W.; Uruga, T.; Ina, T.; Breedlove, B. K.; Yamashita, M., Slow Magnetic Relaxation in a Palladium‐Gadolinium Complex Induced by Electron Density Donation from the Palladium Ion. *Chem. Eur. J.*, **2018**, *24*, 9285-9294; d) Perfetti, M.; Sørensen, M. A.; Hansen, U. B.; Bamberger, H.; Lenz, S.; Hallmen, P. P.; Fennell, T.; Simeoni, G. G.; Arauzo, A.; Bartolomé, J.; Bartolomé, E.; Lefmann, K.; Weihe, H.; Slageren, J.; Bendix, J., Magnetic Anisotropy Switch: Easy Axis to Easy Plane Conversion and Vice Versa. *Adv. Funct. Mater.*, **2018**, *28*, 1801846; e)M Sørensen, M. A.; Hansen, U. B.; Perfetti, M.; Pedersen, K. S.; Bartolomé, E.; Simeoni, G. G.; Mutka, H.; Rols, S.; Jeong, M.; Zivkovic, I.; Retuerto, M.; Arauzo, A.; Bartolomé, J.; Piligkos, S.; Weihe, H.; Doerrer, L. H.; van Slageren, J.; Rønnow, H. M.; Lefmann, K.; Bendix, J., Chemical tunnel-splitting-engineering in a dysprosium-based molecular nanomagnet. *Nat. Commun.*, **2018**, *9*, 1292; f) Yoshida, T.; Izougu, D. C.; Iwasawa, D.; Ogata, S.; Hasegawa, M.; Breedlove, B. K.; Cosquer, G.; Wernsdorfer, W.; Yamashita, M., Multiple Magnetic Relaxation Pathways and Dual-Emission Modulated by a Heterometallic Tb-Pt Bonding Environment. *Chem. Eur. J.*, **2017**, *23*, 10527-10531; g) Yoshida, T.; Cosquer, G.; Izuogu, D. C.; Ohtsu, H.; Kawano, M.; Lan, Y.; Wernsdorfer, W.; Nojiri, H.; Breedlove, B. K.; Yamashita, M., Field-Induced Slow Magnetic Relaxation of GdIII Complex with a Pt−Gd Heterometallic Bond. *Chem. Eur. J.*, **2017**, *23*, 4551–4556; h) Sorensen, M. A.; Weihe, H.; Vinum, M. G.; Mortensen, J. S.; Doerrer, L. H.; Bendix, J., Imposing high-symmetry and tuneable geometry on lanthanide centres with chelating Pt and Pd metalloligands. *Chem. Sci.*, **2017**, *8*, 3566-3575.

(11) a) Xu, W.; Ji, W.-X.; Qiu, Y.-X.; Schwarz, W. H. E.; Wang, S.-G., On structure and bonding of lanthanoid trifluorides LnF_3 (Ln = La to Lu). *Phys. Chem. Chem. Phys.*, **2013**, *15*, 7839-7847; b) Jung, J.; Atanasov, M.; Neese, F., Ab Initio Ligand-Field Theory Analysis and Covalency Trends in Actinide and Lanthanide Free Ions and Octahedral Complexes. *Inorg. Chem.*, **2017**, *56*, 8802-8816; c) Kloditz, R.; Fichter, S.; Kaufmann, S.; Brunner, T. S.; Kaden, P.; Patzschke, M.; Stumpf, T.; Roesky, P. W.; Schmidt, M.; März, J., Series of Tetravalent Actinide Amidinates: Structure Determination and Bonding Analysis. *Inorg. Chem.*, **2020**, DOI: 10.1021/acs.inorgchem.0c01969; d) Hashem, E.;

Swinburne, A. N.; Schulzke, C.; Evans, R. C.; Platts, J. A.; Kerridge, A.; Natrajan, L. S.; Baker, R. J., Emission spectroscopy of uranium(iv) compounds: a combined synthetic, spectroscopic and computational study. *RSC Advances*, **2013**, *3*, 4350-4361; e) Kirker, I.; Kaltsoyannis, N., Does covalency really increase across the 5f series? A comparison of molecular orbital, natural population, spin and electron density analyses of $AnCp_3$ (An = Th–Cm; Cp = η_5-C_5H_5). *Dalton Trans.*, **2011**, *40*, 124-131; f) Zhang, W.-J.; Wang, G.-J.; Zhang, P.; Zou, W.; Hu, S.-X., The decisive role of 4f-covalency in the structural direction and oxidation state of XPrO compounds (X: group 13 to 17 elements). *Phys. Chem. Chem. Phys.*, **2020**, DOI: 10.1039/D0CP04700G; g) Neidig, M. L.; Clark, D. L.; Martin, R. L., Covalency in f-element complexes. *Coord. Chem. Rev.* **2013**, *257*, 394– 406.

(12) a) Pinsky, M.; Avnir. D. Continuous Symmetry Measures. 5. The Classical Polyhedra. *Inorg. Chem.*, **1998**, *37*, 5575–5582.; b) Casanova, D.; Cirera, J.; Llunell, M.; Alemany, P.; Avnir, D.; Alvarez. S. Minimal Distortion Pathways in Polyhedral Rearrangements. *J. Am. Chem. Soc.,* **2004**, *126*, 1755-1763; c) Cirera, J.; Ruiz, E.; Alvarez. S. Shape and Spin State in Four-Coordinate Transition-Metal Complexes: The Case of the d^6 Configuration. *Chem. Eur. J.,* **2006**, *12*, 3162 -3167.

(13) a) Minasian, S. G.; Keith, J. M.; Batista, E. R.; Boland, K. S.; Clark, D. L.; Conradson, S. D.; Kozimor, S. A.; Martin, R. L.; Schwarz, D. E.; Shuh, D. K.; Wagner, G. L.; Wilkerson, M. P.; Wolfsberg, L. E.; Yang, P., Determining Relative f and d Orbital Contributions to M–Cl Covalency in MCl_6^{2-} (M = Ti, Zr, Hf, U) and $UOCl_5$– Using Cl K-Edge X-ray Absorption Spectroscopy and Time-Dependent Density Functional Theory. *J. Am. Chem. Soc.*, **2012**, *134*, 5586-5597; b) Cross, J. N.; Su, J.; Batista, E. R.; Cary, S. K.; Evans, W. J.; Kozimor, S. A.; Mocko, V.; Scott, B. L.; Stein, B. W.; Windorff, C. J.; Yang, P., Covalency in Americium(III) Hexachloride. *J. Am. Chem. Soc.*, **2017**, *139*, 8667-8677.

(14) Choi, Y. G.; Sohn, K.-S.; Kim, K. H.; Park, H. D., Tb L3-edge X-ray Absorption Near-edge Structure Spectroscopic Analysis of Terbium-doped Phosphor Compoundsfor Plasma Display Panel Applications. *J. Mater. Res.* **2011,** *17*, 31-35.

(15) The code can be downloaded at www.neel.cnrs.fr/fdmnes.

(16) a) Tanaka K.; Watanabe N., Study on the Coordination Structure of Pt Sorbed on Bacterial Cells Using X-Ray Absorption Fine Structure Spectroscopy. PLoS One, **2015**, 10, e0127417; b) Coste, S. C.; Pearson, T. J.; Altman, A. B.; Klein, R. A.; Finney, B. A.; Hu, M. Y.; Alp, E. E.; Vlaisavljevich, B.; Freedman, D. E., Orbital energy mismatch engenders high-spin ground states in heterobimetallic complexes.*Chem. Sci.*, **2020**, *11*, 9971-9977; c) Krause, M.; Oliver, Natural widths of atomic *K* and *L* levels, *K*α X ‑ ray lines and several *KLL* Auger lines J. *J. Phys. Chem. Ref. Data*, **1979**, *8*, 329–338.

(17) Huzan, M. S.; Fix, M.; Aramini, M.; Bencok, P.; Mosselmans, J. F. W.; Hayama, S.; Breitner, F. A.; Gee, L. B.; Titus, C. J.; Arrio, M.-A.; Jesche, A.; Baker, M. L., Single-ion magnetism in the extended solid-state: insights from X-ray absorption and emission spectroscopy. *Chem. Sci.* **2020**, *11*, 11801-11810.

(18) a) Tsirelson, V.; Stash, A., Analyzing experimental electron density with the localized-orbital locator. *Acta Crystallographica Section B*, **2002**, *58*, 780-785; b) Zhurova, E. A.; Tsirelson, V. G., Electron density and energy density view on the atomic interactions in $SrTiO_3$. *Acta Crystallographica Section B*, **2002**, *58*, 567-575.

(19) Vlaisavljevich, B.; Miró, P.; Cramer, C. J.; Gagliardi, L.; Infante, I.; Liddle, S. T., On the Nature of Actinide– and Lanthanide–Metal Bonds in Heterobimetallic Compounds. *Chem. Eur. J.* **2011,** *17*, 8424-8433.

(20) Frank, N. The ORCA program system. *Wiley. Interdiscip. Rev. Comput. Mol. Sci.* **2012,** *2,* 73.

(21) Holmberg, R. J.; Ho, L.T. A.; Ungur, L.; Korobkov, I.; Chibotaru, L. F.; Murugesu, M. Observation of unusual slow-relaxation of the magnetisation in a Gd-EDTA chelate. *Dalton Trans.* **2015,** *44*, 20321.

(22) a) Horii, Y.; Katoh, K.; Miyazaki, Y.; Damjanović, M.; Sato, T.; Ungur, L.; Chibotaru, L. F.; Breedlove, B. K.; Nakano, M.; Wernsdorfer, W.; Yamashita, M., Coexistence of spin-lattice relaxation and phonon-bottleneck processes in Gd(III)-phthlocyaninato triple-decker complexes under highly diluted conditions. *Chem. Eur. J.*, **2020**, *26,* 8076-8082; b) Handzlik, G.; Magott, M.; Arczyński, M.; Sheveleva, A. M.; Tuna,

F.; Sarewicz, M.; Osyczka, A.; Rams, M.; Vieru, V.; Chibotaru, L. F.; Pinkowicz, D., Magnetization Dynamics and Coherent Spin Manipulation of a Propeller Gd(III) Complex with the Smallest Helicene Ligand. *J. Phys. Chem. Lett.*, **2020**, *11*, 1508-1515; c) Mayans, J.; Escuer, A. *Chem. Commun.*, **2020**, 10.1039/D0CC07474H.

(23) Stoll, S.; Schweiger, A, EasySpin, a comprehensive software package for spectral simulation and analysis in EPR. *J. Magn. Reson.* **2006**, *178*, 42-55.

(24) Fang, Y.-H.; Liu, Z.; Wang, Y.; Zhou, S.; Jiang, S.; Gao, S., Orientation Mapping of Rabi Frequencies in a Rare-Earth Molecular Qudit. *Inorg. Chem. Front.*, **2020**, *7*, 3875-3881.

(25) Han, T.; Petersen, J. B.; Li, Z.-H.; Zhai, Y.-Q.; Kostopoulos, A.; Ortu, F.; McInnes, E. J. L.; Winpenny, R. E. P.; Zheng, Y.-Z., Dimerized p-Semiquinone Radical Anions Stabilized by a Pair of Rare-Earth Metal Ions. *Inorg. Chem.*, **2020**, *59*, 7371–7375.

(26) AIMAll (Version 19.10.12), Keith, T. A. TK Gristmill Software, Overland Park KS, USA, 2019 (aim.tkgristmill.com).

(27) Stephens, P. J.; Devlin, F. J.; Chabalowski, C. F.; Frisch, M. J., *J. Phys. Chem.,* **1994**, *98*, 11623–11627.

(28) a) Weigend, Florian, Ahlrichs, Reinhart Balanced basis sets of split valence, triple zeta valence and quadruple zeta valence quality for H to Rn: Design and assessment of accuracy. *Phys. Chem. Chem. Phys.,* **2005**, *7*, 3297; b) Andrae, D.; Häußermann, U.; Dolg, M.; Stoll, H.; Preuß, H., Energy-adjusted ab initio pseudopotentials for the second and third row transition elements. *Theor. Chim. Acta*, **1990**, *77*, 123-141; c) Cao, X.; Dolg, M., Segmented contraction scheme for small-core lanthanide pseudopotential basis sets. *J. Mol. Struc-THEOCHEM,* **2002**, *581*, 139-147; d) Dolg, M.; Stoll, H.; Preuss, H., Energy-adjusted ab initio pseudopotentials for the rare earth elements. *J. Chem. Phys*., **1989**, *90*, 1730-1734; e) Dunning, Thom H., Gaussian basis sets for use in correlated molecular calculations. I. The atoms boron through neon and hydrogen. *J. Chem. Phys.*, **1989**, *90*, 1007-1023; f) de Jong, W. A, Harrison, R. J., Dixon, D. A., Parallel Douglas-Kroll energy and gradients in NWChem: Estimating scalar relativistic effects using Douglas-Kroll

contracted basis sets. *J. Chem. Phys.*, **2001**, *114*, 48; g) Kendall, R. A.; Dunning, T. H.; Harrison, R. J. Electron affinities of the first-row atoms revisited. Systematic basis sets and wave functions. *J. Chem. Phys.*, **1992**, *96*, 6796-6806; h) Woon, D. E.; Dunning, T. H., Gaussian basis sets for use in correlated molecular calculations III. The atoms aluminum through argon. *J. Chem. Phys.*, **1993**, *98*, 1358-1371; i) Noro, T.; Sekiya, M.; Koga, T., Sapporo-(DKH3)-nZP (n = D, T, Q) sets for the sixth period s-, d-, and p-block atoms. *Theoretical Chemistry Accounts*, **2013**, *132*, 1363; j) Aravena, D.; Neese, F.; Pantazis, D. A., Improved Segmented All-Electron Relativistically Contracted Basis Sets for the Lanthanides. *J. Chem. Theory Comput.*, **2016**, *12*, 1148-1156.

(29) Stoychev, G. L.; Auer, A. A.; Neese, F. Automatic Generation of Auxiliary Basis Sets. *J. Chem. Theo. Comput.* **2017,** *13*, 554.

(30) Neese, F. *J. Comput.* An improvement of the resolution of the identity approximation for the formation of the Coulomb matrix. *Chem.* **2003,** *24,* 1740.

(31) a) Lu, T.; Chen, F. Multiwfn: A multifunctional wavefunction analyzer. *J. Comput. Chem.*, **2012**, *33*, 580-592; b) K. Momma, F. Izumi, VESTA 3 for three-dimensional visualization of crystal, volumetric and morphology data. *J. Appl. Crystall.* **2011,** *44*, 1272.

(32) Casanova, D.; Llunell, M.; Alemany, P.; Alvarez, S., The Rich Stereochemistry of Eight-Vertex Polyhedra: A Continuous Shape Measures Study. *Chem. Eur. J.*, **2005**, *11*, 1479–1494.

(33) Hernández, M. G.; Beste, A.; Frenking, G.; Illas, F., Charge decomposition analysis of the chemisorption bond. *Chem. Phys. Lett.*, **2000**, *320*, 222-228.

(34) Ravel, B.; Newville, M., *J. Synchrotron Radiat.*, **2005**, *12*,537–541.